ACTA IMEKO
ISSN: 2221-870X
December 2024, Volume 13, Number 4, 1 - 7

Study of photon-counting images compared with energy-integrated images for mammography

Norimitsu Shinohara[1], Toshiyuki Nishihara[1], Shinichi Oguchi[1]

[1] *Department of Radiological Technology, Faculty of Health Sciences, Gifu University of Medical Science, 1-795 Ichihiraga, Nagamine, Seki City, Gifu Seki City, Gifu City, Gifu Prefecture, 501-3892, Japan*

ABSTRACT
High-quality mammographic images are necessary because lesions on mammograms are sometimes difficult for the physician to interpret because they are faint and microscopic. In addition, the breast requires minimal radiation exposure. Current photon counting is energy- integrated images, not photon-counting images, which measures individual photons. In this study, we focused on a mammography system and constructed a novel scheme to experimentally and accurately compare photon-counting images with energy integrated images, where these two types of images are compared at the same total X-ray photon fluence using the same X-ray detection system. In the detecting device, a CsI(Tl) scintillator with columnar crystals is directly glued to the imaging face of an sensitive image sensor. Photon-counting and energy-integrated images were captured with different frame rates and tube currents, while the positional setting of each piece of equipment remained the same. The results showed that the gold discs in the CDMAM3.4 phantom were visually detectable in both energy-integrated and photon-counting images, although the image quality was different, consistent with the simulation. However, our detection devices are small and a larger size is essential for clinical applications.

Section: RESEARCH PAPER

Keywords: Photon-counting image; energy- integrated image; mammography; X-ray; photon

Citation: N. Shinohara, T. Nishihara, Sh. Oguchi, Study of photon-counting images compared with energy-integrated images for mammography, Acta IMEKO, vol. 13 (2024) no. 4, pp. 1-7. DOI: 10.21014/actaimeko.v13i4.1740

Section Editor: Laura Fabbiano, Politecnico di Bari, Italy

Received December 26, 2023; **In final form** November 20, 2024; **Published** December 2024

Funding: This work was supported by the Japan Society for the Promotion of Science (JSPS) KAKENHI, Grant Number 21K12716.

Corresponding author: Norimitsu Shinohara, e-mail: shinohara@u-gifu-ms.ac.jp

1. INTRODUCTION

Breast cancer is the most common cancer among women in Japan, America, and Europe [1]-[3], and mammography is used for population-based breast cancer screening. Microcalcifications and masses are the most important mammographic lesions. The microcalcifications are small pale lesions with a diameter of 50 µm. Masses overlap with normal tissue and mammary glands and are difficult to delineate on mammography. Therefore, these lesions may not be detected by physician interpolation, and high-quality mammographic images are required. Furthermore, the breast is an organ with a high tissue weighting factor that requires minimal exposure to radiation [4], [5].

Photon-counting imaging has attracted attention as an ideal solution for such applications owing to its low noise, high resolution, high (theoretically unlimited) dynamic range and its ability to detect energy of each single X-ray photons. [6]-[8] Several next-generation technologies, such as spectral computed tomography (CT) [9], [10] and photon-counting mammography [11], [12], have been reported.

However, these CT and mammography are conventional energy-integrated images using photon counting, not intrinsic photon-counting with photons measured separately. The photon counting method used in CT and mammography integrates the energy of incident photons per unit area and per unit time. The energy band is then limited, allowing for improved noise characteristics, but also has problems such as the (over) saturation limit of the scintillator. In other words, these devices cannot count individual X-ray photons. This is a limitation that depends on the sensitivity and noise characteristics of the image sensor, and photon-counting images cannot be easily obtained. For this reason, exact experimental comparisons between photon-counting images and conventional energy-integrated images in general have not yet been made because each imaging method requires different X-ray detecting devices with very different features, such as pixel size and quantum efficiency.

There are three advantages of photon-counting images, which count individual X-ray photons.

(1) It has the potential to produce accurate images even at low doses. This has the potential not only to reduce exposure but also to improve the image quality of single-projection images such as breast tomosynthesis.

(2) The accuracy and reliability of the data for material identification can be increased.

(3) It is possible to measure the energy of each X-ray photon, and therefore it may be possible to estimate the nature of the substance from a complete energy profile based on the energy distribution after transmission through the object.

The purpose of this study is to develop a unique X-ray detection system with an order of magnitude increase in sensitivity by incorporating an image sensor [13]-[15] that combines low-noise circuit technology and a photodiode dedicated to light detection, so that not only diagnostic but also mammographic images can be obtained using a new imaging technique that counts individual X-ray photons. In this study, we experimentally attempted to acquire photon-counted and energy-integrated images with the same device under mammographic conditions using a CDMAM 3.4 phantom (Artinis Medical Systems, Elst, The Netherlands). The first attempt to compare these images will be presented.

2. MATERIALS AND METHODS

2.1 X-ray detecting device

The structure of the X-ray detection system is shown in Figure 1. The X-ray detecting device in this study measures 4.9 mm × 3.2 mm (matrix size 320 × 212) and is intended for basic experimental rather than clinical use. The high-sensitivity image sensor used in this study is a CMOS sensor with excellent performance, including a small pixel size of 15 µm pitch and a maximum frame rate of 500 fps.

As shown in Figure 1, a piece of scintillator plate dryly cut out from J6675 (Hamamatsu Photonics, Shizuoka, Japan), which has 150 µm CsI(Tl) columnar crystal layer and 3 mm FOP (Fiber Optic Plate) layer, is directly glued to the imaging face of the sensitive image sensor, forming an indirect photon-counting device. Therefore, unlike conventional silicon image sensors used for indirect X-ray detection, this sensitive image sensor has a fully depleted photodiode in its pixels, which enables an ultrahigh signal conversion ratio for photoelectric charges. Moreover, the sensing circuits are carefully optimized to reduce the readout noise [13]. As a result, the readout noise of each pixel of 15 µm pitch is far less than one electron including dark current shot noise at room temperature. In this study, photon counting images are acquired with this X-ray detector device at very low doses that allow the emission of individual photons to be discriminated, and integral images are acquired at high doses. This means that this X-ray detector system can acquire both photon counting images and integral images with a single device.

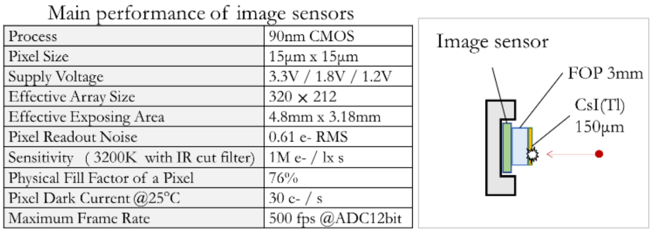

Main performance of image sensors

Process	90nm CMOS
Pixel Size	15µm x 15µm
Supply Voltage	3.3V / 1.8V / 1.2V
Effective Array Size	320 × 212
Effective Exposing Area	4.8mm x 3.18mm
Pixel Readout Noise	0.61 e- RMS
Sensitivity (3200K with IR cut filter)	1M e- / lx s
Physical Fill Factor of a Pixel	76%
Pixel Dark Current @25°C	30 e- / s
Maximum Frame Rate	500 fps @ADC12bit

Figure 1. Features of the sensitive image sensor and schematic image of the X-ray detecting device.

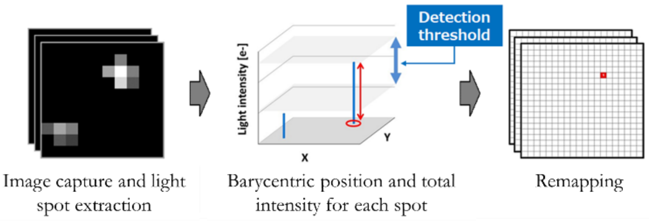

Figure 2. Process of creating a photon-counting image.

2.2 Indirect photon-counting imaging method

The X-ray detecting device used in this study is simply a CMOS Photon Detector. Therefore, it is necessary to image the X-ray detection of the sensitive image sensor as the first process in this study. Figure 2 shows the creation of photon-counting images. When the X-ray detecting device is exposed to X-ray photons, every X-ray photon produces a light spot. From these light spots, the number and incident position of the X-ray photons can be estimated. The energy of the photons can also be estimated from the light intensity. The position of the centre of gravity of several pixel outputs in the light spot is calculated and sorted based on the light intensity threshold. They are then mapped to a logical pixel array in each frame image. Each pixel also has energy data, allowing the energy range of the mapping to be freely selected.

Figure 3 shows an example of light spot extraction from a frame image. First, the average of the dark images was subtracted from each frame image to create clear light-spot images like the first image. Second, the first image is transferred to a binary image using specified pixel output threshold. Then, each light spot is extracted as a bounded area using a flood-fill algorithm [15], resulting in a binary map of extracted light spots shown in the second image. Finally, the barycentric position and the total light intensity of each light spot were calculated using the first image and the second image. Note that the pixel noises are effectively differentiated from the light spots caused by X-ray photons and removed in this extraction process. Thus, at this time, energy sorting is not performed, and we used all extracted photons to create photon-counting images. Our X-ray detection device enables the detection of X-ray photons in photon-counting images by creating them at a high speed of 180 fps. The same device can also produce integral images at a frame rate of 5 fps.

2.3 X-ray tube and experimental settings

Figure 4 shows a schematic of the experimental setup. A Mo foil of 30 um thickness is placed in front of the X-ray tube to adjust the X-ray energy spectrum as an X-ray filter. A CDMAM 3.4 phantom coupled to a 40 mm-thick acrylic board was placed in front of the detecting device. For the X-ray source, we used a

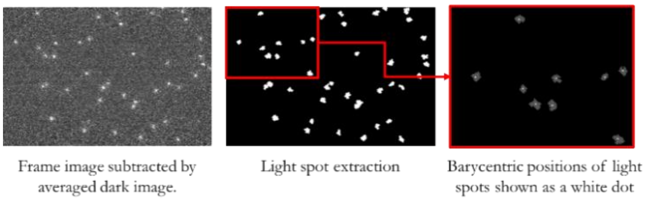

Figure 3. Process of extracting light spots of a single photon.

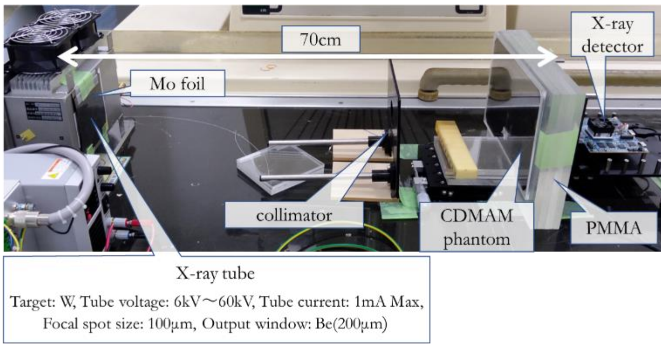

Figure 4. Experimental settings.

XRC6-60 X-ray tube (Mtsusada Precision, Shiga, Japan), whose features are listed on Figure 4 left. This X-ray tube can provide hours of stable low-energy X-ray radiation, enabling the capture of hundreds of thousands of frame images to create photon-counting images. A collimator which has a simple hole is placed between the X-ray tube and the CDMAM phantom to eliminate indirect injection of scattered X-ray photons.

2.4 Estimation and adjustment of the X-ray energy spectrums

We adjusted the experimental X-ray energy spectrum of our X-ray tube with the W target to be practically similar to that of a clinically used mammography equipment with a Mo target. We used MoXS4, developed by Hideki Kato [16], to simulate the energy spectra of the X-ray tubes. The mass attenuation coefficients of the acrylic board, which is usually used as a substitute for human breast, and gold film, which is main content of CDMAM phantom, were obtained using the XCOM database [17], and the attenuations were calculated with an energy step of 0.2 keV.

2.5 Estimation of photon fluence of mammography

Mammography requires low X-ray dosage which strictly restricts total photon fluence detected by X-ray sensors. The quality of X-ray images is affected by both Poisson noise and other noise factors like sensor noise and scintillation noise. If sensors detect photon fluences that are about 100 times larger, the ratio of Poisson noise to the signal decreases to one-tenth. Thus, with very large photon fluence, latter noise factors become dominant and photon-counting-images which can completely eliminate them might have a clear advantage. But in mammography cases, it is essential to examine the balance between the former and the latter.

The photon fluence at the surface of the detecting devices is calculated in actual mammography cases in accordance with the mammography quality control manual in Japan [18], [19], where the maximum average glandular dose) is set at 3.0 mGy. The calculation sequence is shown in Figure 5. First, we determined air kerma based on above mammography guideline, which shows ratio of air kerma to AGD with varied HVL of Al. The air kerma at the surface of the photographic subject was estimated to be approximately 12.5 mGy with a half-value layer (HVL) of 0.43 mmAl. Next, the photon fluence was calculated by referring to the mass energy transfer coefficient of dry air given by Higgins [20]. Subsequently, the subject transmission factor and distance factor were multiplied, resulting in a photon fluence at the surface of the detector at 8.2 × 10^5 mm^{-2}.

2.6 Measurement of photon fluence in the experiment

For the photon-counting images, the photon fluences were directly measured by counting the number of extracted photons.

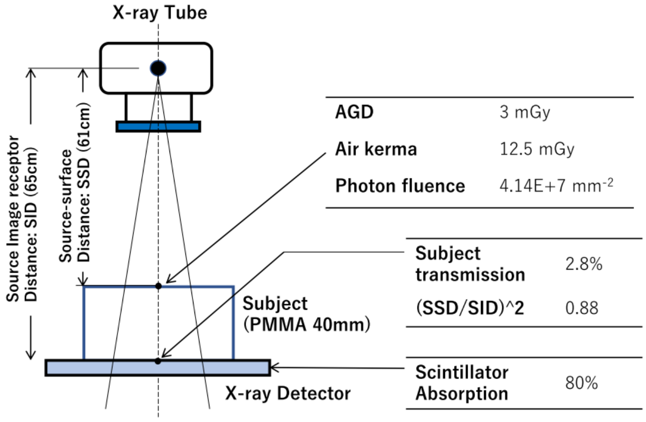

Figure 5. Estimation process of photon fluence in actual mammography.

However, for energy-integrated images, the photon fluences are only estimated by introducing conversion ratio of an X-ray photon to the sensor signal η_p. This factor is determined by measuring the effective sum of sensor signals of arrayed pixels in each frame, which is subtracted from the average sum of the dark signals.

The variance V_s of the sum of the sensor signals in a frame and the average sum A_s of the sensor signals in a frame can be described as follows:

$$V_\mathrm{s} = \eta_\mathrm{p}^2\, V_\mathrm{p} + V_\mathrm{dark} + \eta_\mathrm{e}^2\, V_\mathrm{e} + V_{\eta\mathrm{p}}\, N_\mathrm{p} \tag{1}$$

$$A_\mathrm{s} = \eta_\mathrm{p}\, N_\mathrm{p} = \eta_\mathrm{e}\, N_\mathrm{e} \tag{2}$$

with

V_s [(lsb rms)^2]: variance of the sum of the sensor signals in a frame

A_s [lsb]: average sum of sensor signals in a frame

η_p [lsb]: conversion ratio of an X-ray photon to the sensor signal

V_p [rms^2]: variance in the number of X-ray photons in a frame

V_dark [(lsb rms)^2]: variance of the sum of the dark signals in a frame

η_e [lsb]: conversion ratio of a detected electron to the sensor signal

V_e [rms^2]: variance in the number of detected electrons in a frame

$V_{\eta\mathrm{p}}$ [(lsb rms)^2]: variance of η_p

N_p: average number of X-ray photons in a frame

N_e: average number of detected electrons in a frame.

Equation (1) includes the shot noise of X-ray photons, variance of dark signals, shot noise of scintillated photons converted to electrons in sensor pixels, and variance of the scintillated signals of each X-ray photon.

V_p and N_e are caused by shot noise (Poisson noise) and correspond with the average number of the X-ray photons N_p and the detected electrons N_e respectively

$$V_\mathrm{p} = N_\mathrm{p} \tag{3}$$

$$V_\mathrm{e} = N_\mathrm{e}\,. \tag{4}$$

Our ongoing study on the variation in the scintillated signals of a photon indicates that the fourth factor of equation (1), ($V_{\eta\mathrm{p}}\, N_\mathrm{p}$), is approximately 4 % of the first factor ($\eta_\mathrm{p}^2\, V_\mathrm{p}$). Therefore, we can obtain the variance of frame signals attributed to photon shot noise, $(\eta_{\mathrm{p}}^2\, V_{\mathrm{p}})$, from measured values of V_{s}, V_{dark}, and A_{s}, and the image sensor feature η_{e}.

From equations (2) and (3), we can estimate η_{p} by plotting $(\eta_{\mathrm{p}}^2\, V_{\mathrm{p}})$ versus A_{s}, capturing multiple frame images with different tube currents, where no phantom but the acrylic board was placed.

2.7 Edge profiles and Modulation Transfer Function (MTF)

We conducted edge measurements for both photon-counting and energy-integrated imaging. An acrylic board with a thickness of 40 mm was placed between the edge subject and detecting device.

2.8 Images of CDMAM 3.4 phantom disks

We captured images of CDMAM 3.4 phantom disks with different photon fluences and compared the photon-counting images with energy-integrated images. First, multiple energy-integrated image frames are captured using a tube current of approximately 900 µA and a frame rate of 5 fps. Subsequently, photon-counting image frames are captured using a tube current of approximately 100 µA and a frame rate of 180 fps with the same positional settings. The frame rate for energy-integrated imaging is chosen such that the dark current shot noise is four times larger than the pixel readout noise, and the latter can be neglected.

3. RESULTS

3.1. Estimation and adjustment of the X-ray energy spectrums

As a result of the estimation of the X-ray energy spectrum, the acceleration energy was set to 27 keV and the thickness of the Mo foil to 30 µm. Figure 6 shows the calculated energy spectra and transmission factors of the clinically used and experimental X-rays. The vertical axis represents the relative photon fluence, where the peak photon fluence of the initial X-ray energy profile was set to 1. Although the X-ray from the mammography equipment have two K absorption edges, the total amount of photons in those peaks are very small and overall energy spectrum of the two X-rays are practically the same, which have the same transmission factors. After passing through Poly Methyl Methacrylate (PMMA) with a thickness of 40 mm, the transmission factor of both types of beams for 0.71 µm gold disk is approximately 90%.

	X-ray of a practical mammography equipment Target : Mo 28kV Filter : Mo 30 µm	X-ray used for the experiment Target : W 27kV Filter : Mo 30 µm
Initial X-ray filtered by Mo	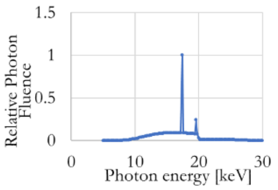	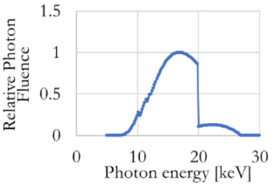
	Transmission factor →	Transmission factor →
X-ray behind PMMA 10mm (breast compression plate)	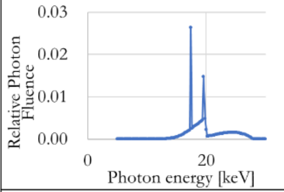	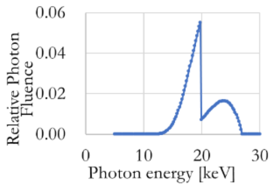
	Photon fluence: 2.8% Energy fluence: 3.4%	Photon fluence: 2.7% Energy fluence: 3.3%
+ PMMA 40mm	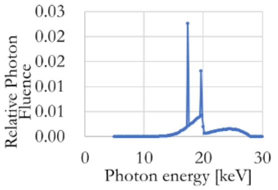	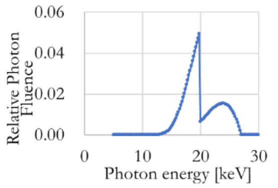
	Photon fluence: 88.8% Energy fluence: 89.4%	Photon fluence: 89.1% Energy fluence: 89.6%

Figure 6. Energy profiles of X-rays where maximum photon fluence of the initial X-rays are set to 1.

3.2. Estimation of photon fluence of mammography

As is described in 2.5., the estimated photon fluence at the surface of the detector is 8.2×10^5 mm^{-2}, and the transmission factor of the subject changed easily with a very slight change in the mass attenuation coefficients or the thickness of the PMMA. However, our detecting device is expected to detect photon fluences of $5 \times 10^5 - 1 \times 10^6$ mm^{-2} in actual mammography cases.

3.3. Measurement of photon fluence in the experiment

As shown in Figure 7, the conversion ratio of the X-ray photons was estimated to be 5287. The small intercept $-2 \cdot 10^{10}$ could be a dark current offset caused by shifted thermal condition of the photon detector.

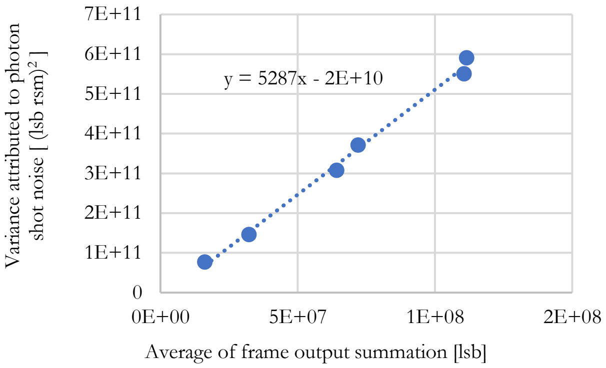

Figure 7. Plotting for the estimation of the conversion ratio of an X-ray photon.

As shown in Figure 8, the photon fluxes detected by photon-counting imaging, which were estimated by photon extraction, and those detected by energy-integrated imaging, which were estimated by the conversion ratio, are plotted with different tube currents. Sufficient consistency in the photon fluxes was

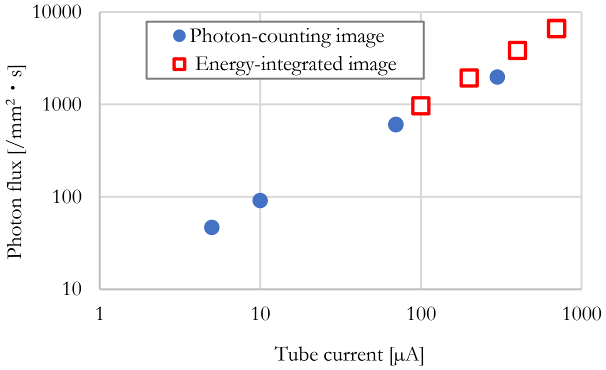

Figure 8. Detected photon flux versus tube current.

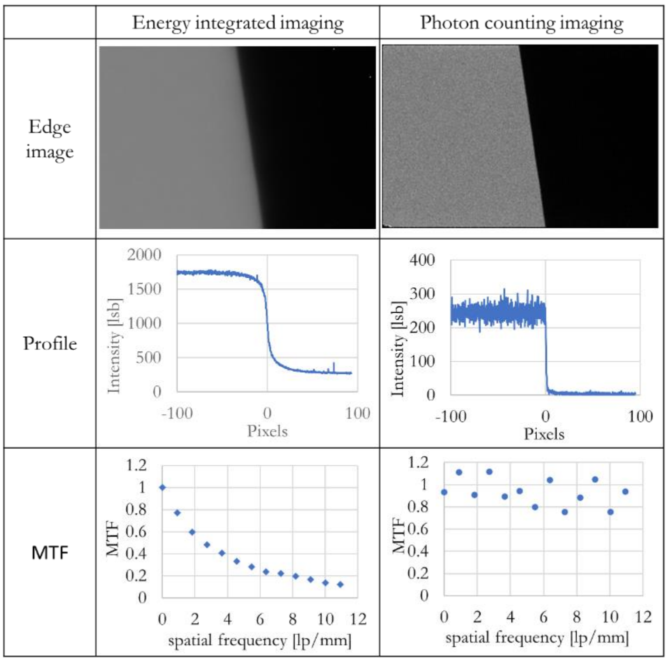

Figure 9. Edge profiles and MTFs of energy-integrated and photon-counting imaging.

observed between both types of imaging, where tube current and all photon fluxes are proportional. Note that with tube current over 100 µA, the density of photons becomes too large to extract every single photon from a frame image, leading to the decrease of the measured photon flux.

This result shows we can match the photon fluence of photon-counting images with that of energy integrated images by matching total current consumption [µA · hour] of our X-ray tube. By adjusting the number of frame images used for the image creation, we can create both photon-counting images and energy integrated images at specified photon fluence.

3.4. Edge profiles and Modulation Transfer Function (MTF)

Figure 9 shows the edge intensity profiles and MTFs. The photon-counting image shows excellent resolution, where the MTF at 10 lp/mm is more than 0.7, whereas the energy-integrated image has an inferior MTF because of light diffusion in the scintillator.

3.5. Images of CDMAM 3.4 phantom disks

Figure 10 shows images of a gold disk with a thickness of 0.71 µm and a diameter of 0.2 mm. Images with different photon fluences were obtained by changing the number of frames used for image construction. The pattern noise of the right peripheral area of the photon-counting images originates from the incomplete bonding surface of the scintillator, which cannot be fully compensated by white image calibration.

In the photon-counting images, the background noise increased with a decrease in photon fluence. The photon-counting images show a sharp contrast, but the visibilities are deteriorated by Poisson noise. The energy-integrated image has a blurred disc image and blurred background noise due to the effect of light diffusion in CsI(Tl) [21]. However, the photon-counting image had poor noise characteristics, and the energy-integrated image had poor resolution characteristics, but the same gold disks could be imaged and were visible.

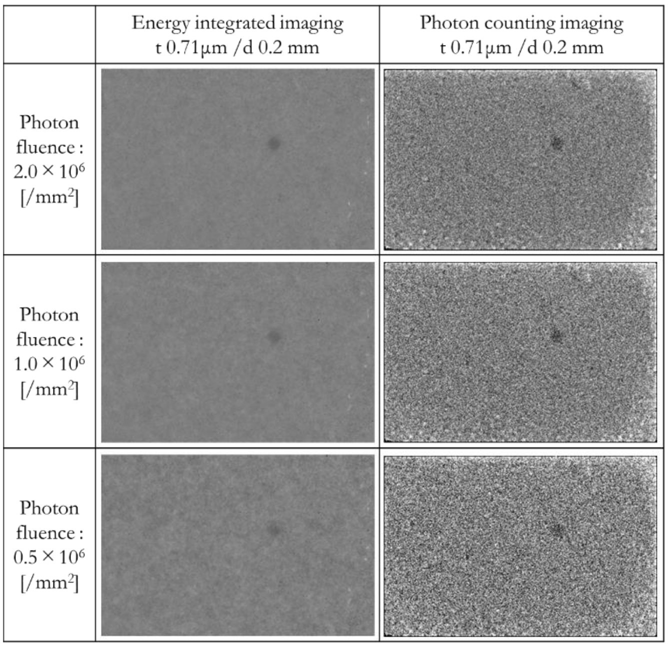

Figure 10. Images of a gold disk with a thickness of 0.71 µm and a diameter of 0.2 mm.

In Figure 11, the images of 0.71-µm-thick gold disks with diameters of 0.1 mm are shown with three levels of photon fluences. When the photon fluence is reduced to 5.0 × 10^5 m^{-2}, the disk Figure of 0.1 mm diameter cannot be distinguished from the background noise in both the photon-counting and energy-integrated images.

Although the image quality was different for images shown in Figure 10 and Figure 11, the photon-counting images and energy-integrated images confirmed that the gold discs could be detected visually.

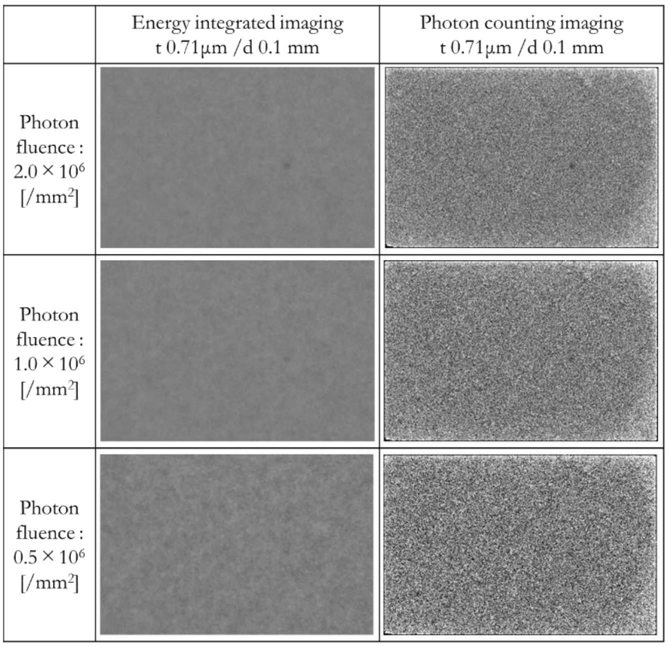

Figure 11. Images of a gold disk with a thickness of 0.71 µm and a diameter of 0.1 mm.

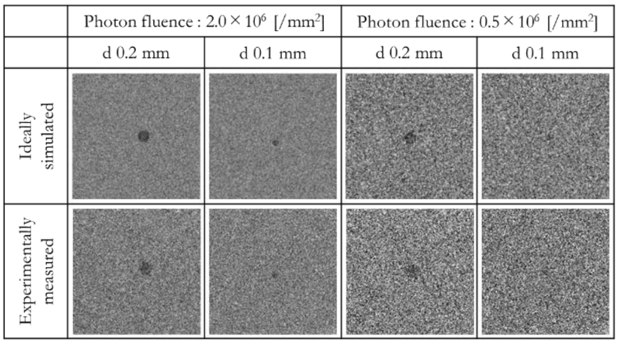

Figure 12. Experimentally measured photon-counting images are compared with simulated ones.

4. DISCUSSION

In Figure 12, photon-counting images in Figure 10 and Figure 11 are compared with simulated ideal photon-counting images, where the transmission factor of gold of 0.71 μm thickness is set to 90 % and is created by generating random numbers of Poisson distribution. When the photon fluence was 2.0×10^6 mm^{-2}, the experimental images showed inferior background noise because of incomplete white pattern noise calibration. However, with a photon fluence of 5.0×10^5 mm^{-2}, the Poisson noise becomes larger and dominant, leading to experimental images having almost the same quality as the simulated images. Therefore, the experimental photon-counting images and energy-integrated images acquired in the study were considered to be in line with our estimates.

Photon counting and energy-integrated images were acquired with the same detecting device and the same X-ray photon fluence. In both images, the gold discs in the CDMAM 3.4 phantom were detectable under actual mammographic conditions.

The inferior noise characteristics of the photon counting images were mainly due to the large number of frames and were strongly influenced by Poisson noise. In the present study, photon counting images and energy-integrated images were acquired separately. However, it is possible to create an image by integrating the frames of the photon counting image. Therefore, it is possible to acquire different features of the photon counting image and the energy-integrated image in one shot. Furthermore, photon counting images, which detect individual X-photons, have the potential to improve the accuracy of conventional energy-integrated images.

The limitation of this study is that our detecting devices are small at 4.9 mm × 3.2 mm (matrix size 326 × 216). Therefore, they cannot be used as clinical devices. Research is currently underway to increase the size of the sensor by tiling [22]. Furthermore, only a few image samples have been taken so far and the assessment of visibility is qualitative. More images with different gold thicknesses need to be obtained to reach solid conclusions.

For quantitative studies, we plan to extract the Point spread function (PSF) of the scintillator from multiple single-photon images, which might explain the MTF of the energy-integrated images shown in Figure 9, as indicated by a previous study using an Electron Multiplying Charge Coupled Device (EMCCD) coupled with an image intensifier [21]. A precise quantitative noise evaluation using Noise power spectrum (NPS) should also be performed.

Our ultimate goal is to determine the practical advantages of photon-counting imaging and draw up a scenario to take them for its use in mammography. Our basic experimental next step will be to study the energy discrimination of X-ray photons.

5. CONCLUSIONS

In this study, basic experiments were carried out on an X-ray detector for mammography that is capable of capturing both photon-counted and integral images by means of an image sensor combining low-noise circuit technology and a photodiode dedicated to light detection. This study reports the first acquisition of photon-counted and energy-integrated images with the same detecting device and the same X-ray photon fluence. Gold discs in the CDMAM 3.4 phantom were visually detectable in both images under actual mammographic conditions, in agreement with simulated the results were in agreement with the simulation. The possibility of integrating frames of photon-counting images to create an integral image is feasible, suggesting new imaging possibilities.

However, our detecting devices are small in size, and it is essential to increase the size for clinical applications. The present study is a qualitative evaluation based on visual images, and quantitative evaluation should also be pursued.

REFERENCES

[1] National Cancer Center Japan, Cancer information service. Online [Accessed November 2023] https://ganjoho.jp/reg_stat/statistics/stat/summary.html

[2] The Surveillance, Epidemiology and End Results (SEER), Cancer Stat Facts: Common Cancer Sites. Online [Accessed November 2023] https://seer.cancer.gov/statfacts/html/common.html

[3] International Agency for Research on Cancer, CANCER TODAY. Online [Accessed November 2023] http://gco.iarc.fr/today/home

[4] ICRP. Use of dose quantities in radiological protection, ICRP Publication 147, Ann. ICRP, 2021; 50 (1).

[5] ICRP. The 2007 Recommendations of the International Commission on Radiological Protection, ICRP Publication 103, Ann. ICRP, 2007, 37 (4).

[6] A. Shankar, J. Krebs, D. R. Bednarek, S. Rudin, Spectroscopy with a CdTe-based photon-counting imaging detector (PCD) having charge sharing correction capability, Medical Imaging 2018: Physics of Medical Imaging, Vol. 10573, 2018, pp. 1287-1294. DOI: https://doi.org/10.1117/12.2294632

[7] E. N. Gimenez, R. Ballabriga, M. Campbell (+ another 6 authors), Study of charge-sharing in MEDIPIX3 using a micro-focused synchrotron beam, Journal of Instrumentation, 6(01): 2011, C01031.
DOI: https://doi.org/10.1088/1748-0221/6/01/C01031

[8] J. Dudak, High-resolution X-ray imaging applications of hybrid-pixel photon counting detectors Timepix, Radiation Measurements, 137: 2020, 106409.
https://doi.org/10.1016/j.radmeas.2020.106409

[9] J. S. Iwanczyk, E. Nygard, O. Meirav, J. Arenson, W. C. Barber, N. E. Hartsough, N. Malakhov, J. C. Wessel, Photon Counting Energy Dispersive Detector Arrays for X-ray Imaging, IEEE Transactions on Nuclear Science, 56(3): 2009, pp. 535-542. DOI: https://doi.org/10.1109/TNS.2009.2013709

[10] N. J. A. Scott, N. J. Cook, J. S. Butzer (+ another 6 authors), Spectroscopic (multi-energy) CT distinguishes iodine and barium contrast material in MICE. European Radiology, 20(9): 2010, pp. 2126-2134.
DOI: https://doi.org/10.1007/s00330-010-1768-9

[11] R. Suzuki, A. Nakajima, M. Sasaki (+ another 9 authors), A proposed new image display method with high contrast-to-noise

ratio using energy resolved photon-counting mammography with a CdTe series detector, Proc. SPIE 10573, 2018, Medical Imaging: 105735K1-105735K6.
DOI: https://doi.org/10.1117/12.2292871

[12] H. Jiang, J. Kaercher, R. Durst, Indirect-detection single-photon counting x-ray detector for breast tomosynthesis, Proc. SPIE 9783. 2016, Medical Imaging; 9783P.
DOI: https://doi.org/10.1117/12.2217115

[13] T. Nishihara, M. Matsumura, T. Imoto (+ another 7 authors), An Experimental CMOS Photon Detector with 0.5e- RMS Temporal Noise and 15µm pitch Active Sensor Pixels, IEDM Digest Tech. Papers, 2017, 16.1, pp. 1-4.
DOI: https://doi.org/10.1109/IEDM.2017.8268400

[14] T. Nishihara, H. Baba, M. Matsumura, O. Kumagai, T. Izawa, Indirect photon-counting x-ray imaging using CMOS Photon Detector (CPD), Proc. SPIE 10948, 2019, Medical Imaging: 109481U1-109481U-9.
DOI: https://doi.org/10.1117/12.2510996

[15] T. Nishihara, H. Baba, O. Kumagai, T. Izawa, N. Shinohara, A study of energy resolution in CPD indirect photon-counting x-ray imaging, Proc. SPIE 11312. 2020, Medical Imaging: 113120D.
DOI: http://dx.doi.org/10.1117/12.2548885

[16] Laboratory of Radiological Technology. Online [Accesses September 2023]
https://hidekikato1952.wixsite.com/radiotechnology

[17] NIST, XCOM data base. Online [Accesses November 2023]
https://www.physics.nist.gov/PhysRefData/Xcom/html/xcom1.html

[18] Mammography Guideline Diffusion Team. Radiography Section, Japanese Society of Radiological Technology: Radiological Technology Library (14-4) Nyubo Satsuei Seido Kanri Manuaru Kaiteiban (Mammography Quality Control Manual, Revised Edition). 2012, Japanese Society of Radiological Technology, Kyoto. [in Japanese]

[19] Japan Radiological Society and Japanese Society of Radiological Technology. Mammography Guideline the third enlarged edition. 2014, IGAKU-SHOIN Ltd., Tokyo. [in Japanese]

[20] P. D. Higgins, F. H. Attix, J. H. Hubbell, S. M. Seitzer, M. J. Berger, C. H. Sibata, Mass energy transfer and mass energy-absorption coefficients including in-flight positron annihilation for photon energy 1 keV to 100 MeV, NISTIR 4812, 1992, National Bureau of Standards, Washington D.C. Online [Accessed 13 December 2024]
https://archive.org/details/massenergytransf4812higg

[21] A. Howansky, A. R. Lubinsky, S. K. Ghose, K. Suzuki, W. Zhao, Direct measurement of Lubberts effect in CsI(Tl):Tl scintillators using single x-ray photon imaging, Proc. SPIE 10132, 2017, Medical Imaging: 1013209.
DOI: https://doi.org/10.1117/12.2255561

[22] B. Jacob, H. Vafi, B. D. Yanoff, J. J. Shaw, J. Guo, Radiation detector assembly, US Patent US2017/019374 A1. Online [Accessed 13 December 2024]
https://patents.google.com/patent/US20170194375A1/en